NANO LETTERS

pubs.acs.org/NanoLett Letter

Intertwined Topological and Magnetic Orders in Atomically Thin Chern Insulator $MnBi_2Te_4$

Dmitry Ovchinnikov, Xiong Huang, Zhong Lin, Zaiyao Fei, Jiaqi Cai, Tiancheng Song, Minhao He, Qianni Jiang, Chong Wang, Hao Li, Yayu Wang, Yang Wu, Di Xiao, Jiun-Haw Chu, Jiaqiang Yan,* Cui-Zu Chang,* Yong-Tao Cui,* and Xiaodong Xu*

Cite This: *Nano Lett.* 2021, 21, 2544−2550 Read Online

ACCESS | Metrics & More | Article Recommendations | Supporting Information

ABSTRACT: $MnBi_2Te_4$, a van der Waals magnet, is an emergent platform for exploring Chern insulator physics. Its layered antiferromagnetic order was predicted to enable even−odd layer number dependent topological states. Furthermore, it becomes a Chern insulator when all spins are aligned by an applied magnetic field. However, the evolution of the bulk electronic structure as the magnetic state is continuously tuned and its dependence on layer number remains unexplored. Here, employing multimodal probes, we establish one-to-one correspondence between bulk electronic structure, magnetic state, topological order, and layer thickness in atomically thin $MnBi_2Te_4$ devices. As the magnetic state is tuned through the canted magnetic phase, we observe a band crossing, i.e., the closing and reopening of the bulk band gap, corresponding to the concurrent topological phase transition in both even- and odd-layer-number devices. Our findings shed new light on the interplay between band topology and magnetic order in this newly discovered topological magnet.

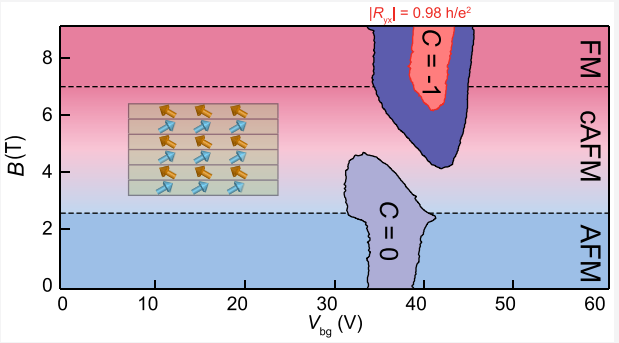

KEYWORDS: *band-crossing, topological magnets, Chern insulator, chiral edge states*

Chern insulators, which are quantum Hall insulators without the formation of Landau levels, possess quantized Hall conductance with dissipation-free chiral edge states.[1] The interplay between topological physics and time reversal symmetry breaking is a prerequisite for the realization of the Chern insulator state.[2] So far, the Chern insulator state has been experimentally realized in magnetically doped topological insulator thin films/heterostructures[3−9] and the recently discovered twisted graphene moiré systems.[10−12]

Recently, van der Waals magnet $MnBi_2Te_4$ has emerged as a new system to realize the Chern insulator state.[13−21] In contrast to existing systems,[3−9] whose parent materials have no intrinsic magnetic order, $MnBi_2Te_4$ is an intrinsic layered antiferromagnet (AFM).[13,14] The adjacent ferromagnetic (FM) monolayers with out-of-plane magnetization are AFM coupled, which can be further driven into a canted antiferromagnetic (cAFM) and FM states by applying a magnetic field (Figure 1a). The coupling of different magnetic configurations to the topological states are predicted to lead to a variety of topological phenomena.[19−21] For instance, in the AFM ground state, an odd-layer sample possesses effectively one net layer of uncompensated magnetization and is predicted to host the QAH state, while the magnetization is fully compensated for in an even-layer sample, which is expected to be an axion insulator.[19−21] Experimentally, using exfoliated atomically thin devices, gate tunable quantized Hall resistance with a Chern number $C = -1$ has been observed in the magnetic-field-driven FM states[15−18] as well as at zero magnetic field in an odd-layer-number device.[15]

These promising results point to atomically thin $MnBi_2Te_4$ as a desirable platform to study the correlation between band topology and magnetic order. So far, experiments have focused on edge transport, and the corresponding magnetic states are usually inferred from Hall measurements. Direct correlation between magnetic and topological orders has yet to be established. It is also unclear how the bulk electronic band structure evolves as the magnetic state is tuned, and how the even−odd layer number effects are manifested during the topological phase transition (TPT), which is unique to this layered AFM system.

In this work, we unravel the intertwined band topology and magnetic order as a function of $MnBi_2Te_4$ layer thickness. This

Received: December 29, 2020
Revised: March 8, 2021
Published: March 12, 2021

https://dx.doi.org/10.1021/acs.nanolett.0c05117
Nano Lett. 2021, 21, 2544−2550

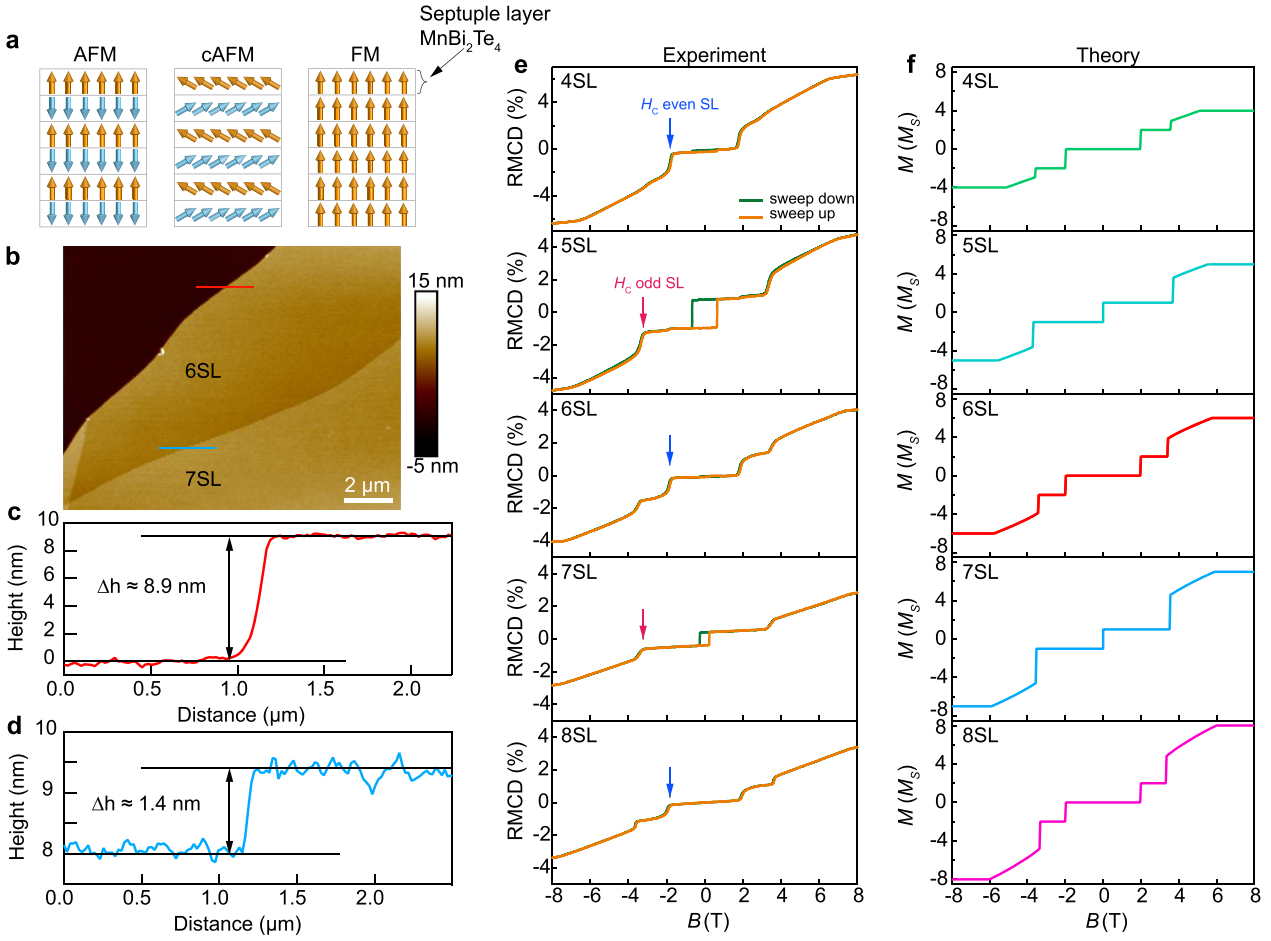

Figure 1. Layer-dependent magnetic order in thin flakes of $MnBi_2Te_4$. (a) Schematics of magnetic order evolution as a function of magnetic field. From left to right: antiferromagnetic (AFM), canted antiferromagnetic (cAFM), and ferromagnetic (FM) states, which consequently form under an increase of perpendicular magnetic field, *B*. (b) Atomic force microscopy (afm) micrograph of freshly exfoliated $MnBi_2Te_4$ flakes with thicknesses of 6 SL and 7 SL. (c, d) Height profiles across the lines, denoted with corresponding colors in panel b. (d) Data showing a single SL step size of 1.4 nm. (e) Reflective magnetic circular dichroism (RCMD) measurements as a function of magnetic field for 4 SL to 8 SL flakes at $T = 2$ K. All samples are freshly exfoliated and not covered by PMMA. (f) Theoretical modeling of the magnetization with respect to external magnetic field for 4−8 SL flakes.

is achieved by employing reflective magnetic circular dichroism (RMCD) to identify magnetic states, scanning microwave impedance microscopy (MIM) to image edge conduction and measure local bulk conductivity, and electrical transport to measure bulk resistance as well as the topological invariant via anomalous Hall traces. Our devices are fabricated using mechanically exfoliated $MnBi_2Te_4$ thin flakes (see Methods in the Supporting Information (SI)). Figure 1b shows atomic force microscopy micrographs of adjacent 6 and 7 septuple layer (SL) flakes. The line cut in Figure 1c shows the thickness of the 6 SL flake. The single SL step between those two flakes is ∼1.4 nm thick, consistent with prior reports.[15−17]

Since the even- and odd-layer samples have compensated and uncompensated magnetic moments, respectively, the total magnetization should exhibit distinct magnetic-field dependence. We first investigate this even−odd effect by RMCD measurements (see SI Methods). Figure 1e illustrates the RMCD signal for flakes with thicknesses from 4 to 8 SL. Two major differences in RMCD signal between even and odd layers stand out. First, odd SL flakes have pronounced hysteresis loops and significant remanent RMCD signals in the AFM state, which results from the uncompensated magnetic moments, while even layers have vanishingly small RMCD signals and hysteresis loops, consistent with their zero net magnetization. Second, the critical magnetic field for the spin−flop transition between the AFM and cAFM states, labeled by H_C with blue and red arrows in Figure 1e, is about 1.8 T for even-SL flakes, which is distinct from the value of ∼3.8 T for odd SL flakes. Our RMCD results are qualitatively consistent with a recent preprint.[22] The larger H_C for odd SL compared to the even ones can be explained by the Zeeman energy of the uncompensated magnetization in the former case, which stabilizes the AFM state. This even−odd layer dependent RMCD signal is well captured by our theoretical modeling of *M* vs *B* field (Figure 1f, see SI Methods for calculation details) and appears to be a reliable way to distinguish between even and odd SL flakes.

We next investigate the correlation between magnetic states and the Chern number, *C*, in both even and odd SL $MnBi_2Te_4$ devices. We show such a side-by-side comparison between a 6 SL (Figure 2a−c) and a 5 SL (Figure 2d−f) device. Overall, the RMCD signals of the devices are consistent with the freshly cleaved flakes (Figure 1e). For the 6 SL device (6SL-1), RMCD signal in the AFM state nearly vanishes, although a tiny hysteresis loop exists (Figure 2a), which does not appear in freshly cleaved 6-SL samples. We speculate that its formation is

https://dx.doi.org/10.1021/acs.nanolett.0c05117
Nano Lett. 2021, 21, 2544−2550

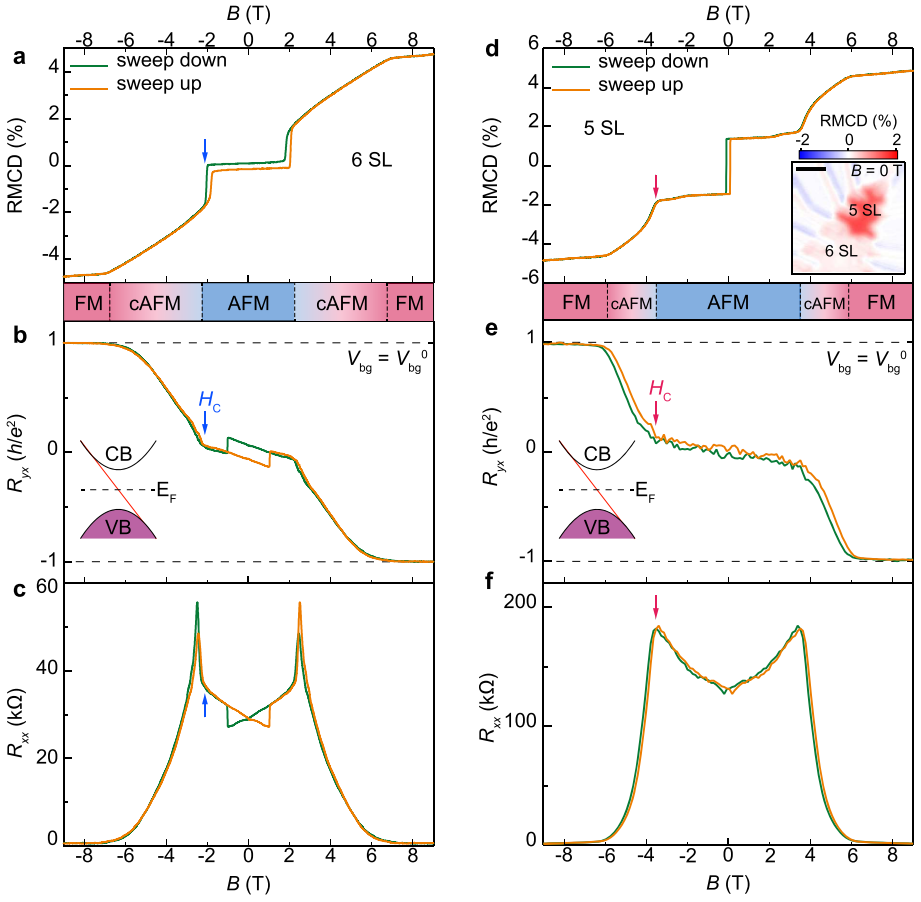

Figure 2. Correlation of magnetic and topological properties of even and odd SL $MnBi_2Te_4$ flakes. (a) RMCD signal, (b) antisymmetrized Hall resistance, R_{yx}, (c) symmetrized longitudinal resistance, R_{xx}, as a function of magnetic field in device 6SL-1 at T = 2 K. See Figure S1 for the raw data. Transport and RMCD measurements were taken at $V_{bg} = V_{bg}^0$ = 37 V and V_{bg} = 0 V, respectively. (d) RMCD signal, (e) R_{yx}, (f) R_{xx}, as a function of magnetic field of device 5SL-1. Transport measurements were taken at $V_{bg} = V_{bg}^0$ = 44.4 V. Inset in panel d: RMCD map taken at zero magnetic field, showing a single magnetic domain for the 5SL-1 device. Scale bar in the inset: 10 μm. Insets in panels b and e: chiral edge state dispersions in the FM state.

likely a result of uncompensated magnetization initiated by fabrication (Figure S2), which is often seen in 2D layered antiferromagnet CrI_3.[23] The odd-layer device 5SL-1 has an expected hysteresis loop centered around B = 0 T (Figure 2d). The sharp transition is the signature of a spin−flip transition between two magnetic states with the same net magnetic moment but opposite signs. The remnant RMCD signal is about 28% of that in the FM state, which is slightly larger than the expected value of 20%. The RMCD map under B = 0 T also shows a uniform signal (Figure 2d, inset), suggesting large magnetic domains.[22,24]

The transport signal shows that the spin−flop fields, determined by the rising point of R_{yx}, are consistent with the RMCD measurements. For both devices, a Chern insulator state of C = −1 is observed in the magnetic-field-induced FM state when B > 6 T, made evident by quantized Hall resistance $R_{yx} = -h/e^2$ (Figure 2b,e) and vanishing longitudinal resistance R_{xx} (Figure 2c,f). These are consistent with prior reports.[15−18] In the AFM state of the even-layer device (6SL-1) at B < ∼2 T, R_{yx} is small while R_{xx} is large. Although RMCD nearly vanishes, R_{yx} has a small hysteresis loop with a coercive field that differs from that measured by RMCD. From our spatially resolved RMCD measurements, small hysteresis loops similar to those in R_{yx} are observed for some spots near the sample edges, suggesting that the loops might be caused by imperfections near the edge of the device (Figure S2). Unexpectedly, for the odd-layer device (5SL-1) in the AFM state at $|B| < H_C \sim 3.8$ T, both R_{yx} and its hysteresis loop nearly vanish, in stark contrast to the observed uncompensated magnetic moment and pronounced hysteresis in RMCD. In addition to the close-to-zero R_{yx}, R_{xx} reaches a large value of about 7 h/e^2. Our results suggest that the AFM state in our 5-SL device is likely a trivial magnetic insulator in which a vanishing R_{yx} is expected. We note that existing experimental works report different results regarding odd-layer-number samples.[15−18] The origin of the trivial insulator state in the AFM state in many reported odd-layer-number samples,[15−18] which appears to be opposite to theoretical predictions,[19−21] remains to be carefully investigated.

After comparing the even−odd layer number effects in the FM and AFM states, we turn our attention to the evolution of bulk electronic structure during the magnetic-field-driven TPT in the cAFM states. We find that both even- and odd-SL devices exhibit a similar band-crossing behavior, with subtle variations due to their differing magnetization vs B-field behaviors (see Figures S3 and S4 for data on two 5-SL devices). To probe the bulk states, we measure the local conductivity of the sample bulk by MIM. Using a 6 SL device (6SL-2) as an example, a metal tip is scanned across the sample and the complex impedance between the tip and sample is

https://dx.doi.org/10.1021/acs.nanolett.0c05117
Nano Lett. 2021, 21, 2544−2550

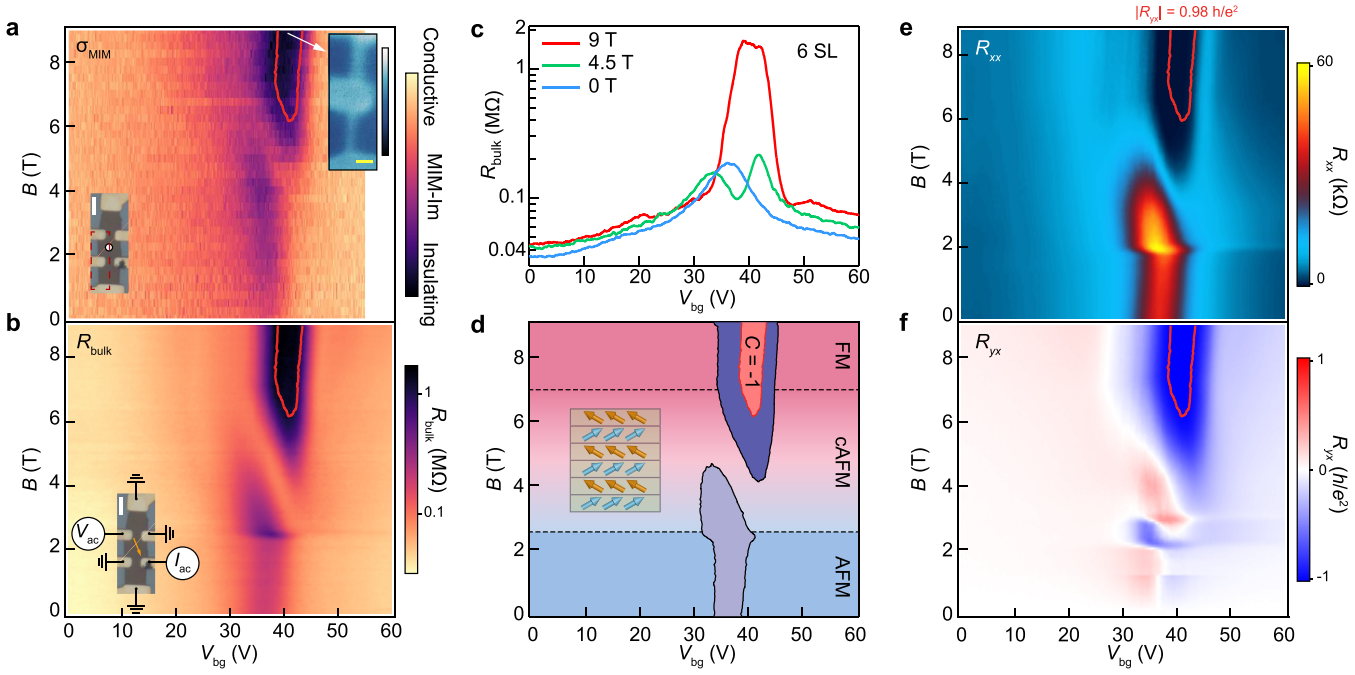

Figure 3. Probing band crossing during the topological phase transition and imaging of Chern gap in a 6 SL device. (a) V_{bg}−B map of the MIM-Im signal measured inside the bulk (indicated by the white dot in the lower inset; scale bar, 5 μm), labeled as σ_{MIM}, taken at T = 3 K. Upper inset (scale bar, 2 μm): spatial MIM scan of the device region outlined by the red dotted rectangle in the lower inset, taken in the Chern insulator state at B = 9 T and T = 3 K. (b) V_{bg}−B map (log scale) of the bulk resistance, R_{bulk}, taken at T = 2 K. Inset: measurement configuration. Scale bar: 5 μm. (c) Line cuts of R_{bulk} vs V_{bg} at B = 0, 4.5, and 9 T, extracted from panel b. (d) Phase diagram of the topological phase transition. The contours of R_{bulk} = 150 kΩ (black solid lines) indicate the regions of the bulk insulating states in both the AFM and FM states. The contour of $|R_{yx}|$ = 0.98 h/e^2 (red solid line), determined from panel f, indicates the C = −1 Chern insulator region. Inset: schematics of the cAFM phase during the topological phase transition. (e, f) V_{bg}−B maps of (e) the raw longitudinal resistance, R_{xx}, and (f) the antisymmetrized Hall resistance R_{yx}, taken at T = 2 K. The contour of $|R_{yx}|$ = 0.98 h/e^2 is overlaid in panels a, b, d, e, and f. All data shown here are from device 6SL-2.

measured. The real and imaginary parts of the MIM response, MIM-Im and MIM-Re, are used to analyze the sample conductivity.[25] In particular, the MIM-Im channel, which characterizes the ability of the sample to screen the electric field from the tip, increases monotonically with the local conductivity. To avoid edge contribution, we measure the MIM signal of bulk by parking the tip near the center of the flake, ∼4 μm away from the edge (Figure 3a, inset). Figure 3a shows the intensity plot of the MIM-Im signal, σ_{MIM}, as a function of B and V_{bg}. In addition, we measure bulk resistance, R_{bulk}, via transport using the contact configuration illustrated in the inset of Figure 3b. We apply a small AC voltage bias between a pair of electrodes on opposite sides of the Hall bar while grounding all other electrodes. Since the edge conduction is grounded, the current mainly goes through the sample bulk (see SI Methods). The V_{bg}−B map of R_{bulk} is shown in Figure 3b. To correlate the bulk states with the topological properties, the V_{bg}−B maps of R_{xx} and R_{yx} are also measured (Figure 3e,f).

These four maps of complementary quantities show striking similarities in the V_{bg} and B dependence, which reveals the evolution of the bulk electronic structure during the magnetic-field-induced TPT. Importantly, the local (Figure 3a) and bulk (Figure 3b) resistance maps match well, demonstrating the robustness of our measurements on the bulk electronic states. These two maps show that, in both the AFM (B < 2 T) and FM (B > 6 T) regimes, there is a resistive state within a certain gate range (see also the line cuts of R_{bulk} vs V_{bg} at selected B in Figure 3c). These resistive states correspond to the range of V_{bg} where the Fermi level is tuned inside the bulk band gap (Figure 3d). Upon comparison to the R_{xx} and R_{yx} maps, we can see that the bulk gap in the AFM state corresponds to the C = 0 insulating state, which has close-to-zero R_{yx} and large R_{xx}, implying its trivial origin. In contrast, the highly insulating bulk state in the FM state at high fields coincides with the gate range for quantized R_{yx} and vanishing R_{xx} (Figure 3e,f). Overlaying the contour of R_{yx} at a threshold of 98% of $-h/e^2$ on all maps displays an excellent correlation among all four data sets. Furthermore, spatial MIM scans reveal the formation of conductive edge states in this regime (see the upper inset of Figure 3a and Figure S5 for a complete MIM image set showing the evolution of spatial conductivity profiles near the edges). All of these measurements mark the observation of the Chern insulator gap with C = −1 in the FM phase.

The cAFM phase connects the C = 0 insulating state in the AFM phase to the C = −1 Chern insulator in the FM phase. The σ_{MIM} and R_{bulk} maps show that as B increases above ∼2 T, the gate regime for the C = 0 insulating state shrinks while an incipient Chern insulator gap appears and increases, with a conductive state separating the two regimes. Specifically, as B increases, one bulk conduction band of the AFM phase splits off and moves toward the bulk valence band. Eventually, it crosses the entire band gap and merges with the bulk valence band at B ∼ 7 T in the FM phase (Figure 3d). Meanwhile, the Chern insulator gap increases and eventually fully opens, accompanying the gradual increase of $|R_{yx}|$ to the quantized value of h/e^2 and the decrease of R_{xx} toward zero. Therefore, what we observe is the band-crossing process, where canting of the magnetic moment is responsible for the energy shift of the crossing band via exchange interaction. The same band-

https://dx.doi.org/10.1021/acs.nanolett.0c05117
Nano Lett. 2021, 21, 2544−2550

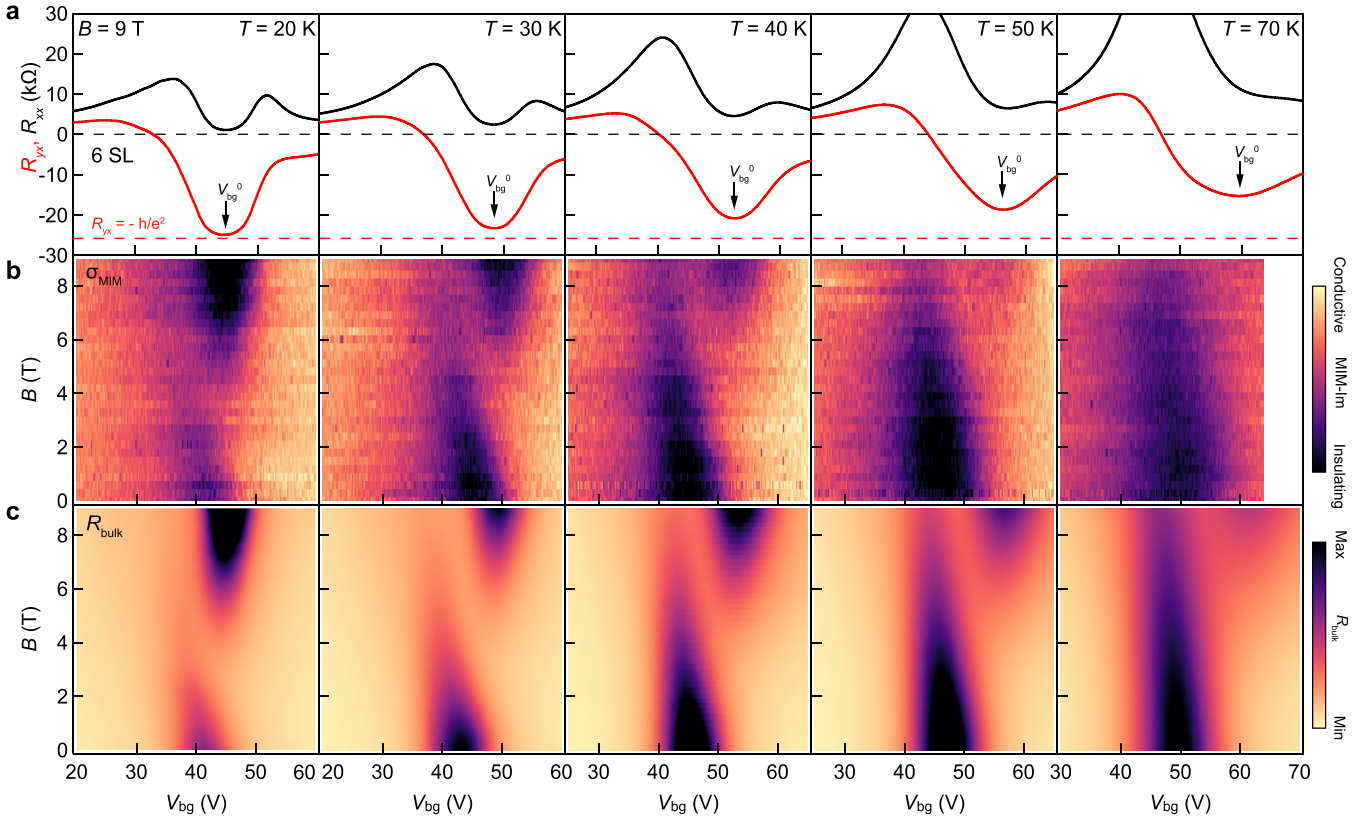

Figure 4. Temperature dependence of the band crossing and Chern insulator state. All data shown here are from device 6SL-2. (a) R_{xx} (symmetrized) and R_{yx} (antisymmetrized) vs V_{bg} curves at B = 9 T and selected temperatures. (b, c) Corresponding V_{bg}−B maps of (b) the bulk MIM-Im signal and (c) R_{bulk}. The color scale for each panel is adjusted to highlight the band-crossing feature.

crossing process is observed in both even- and odd-layer devices, as it is evident by comparing Figure 3 and Figure S3, which underlines direct and robust connection between magnetic state and topological state of $MnBi_2Te_4$.

Finally, we investigate the temperature dependence of the band crossing and Chern insulator gap to examine their correlation with the formation of the magnetic order. Figure 4 illustrates the temperature dependence of the electronic properties in device 6SL-2. (Results of 5SL-1 with a similar temperature dependence are presented in Figure S6.) Our thin flakes of $MnBi_2Te_4$ typically have a magnetic ordering temperature $T_N \sim 23$ K (Figure S7). Figure 4a shows the R_{yx} and R_{xx} as a function of V_{bg} at B = 9 T at selected temperatures. We correlate the transport measurements with the band-crossing feature probed by σ_{MIM} and R_{bulk} (Figure 4b,c, and see also Figure S8 for edge states measured at all temperatures). At T = 20 K and below, the band crossing occurs in the B range between 2 and 7 T. At T = 30 K, the splitting of the sub-band from the conduction band starts at a higher B and the band shift becomes more gradual. At B = 9 T, the crossing branch touches the bulk valence band without a complete merge. There is a close-to-quantization region where R_{yx} is still as high as 90% of h/e^2 and R_{xx} remains low, indicating the persistence of the chiral edge state. At T = 40 K, the close-to-quantization region shrinks further with a maximum of $R_{yx} \sim 0.8\ h/e^2$ and the crossing band barely touches the bulk valence band at B = 9 T. The large Hall angle R_{yx}/R_{xx} at temperatures above T_N is similar to a recent report,[17] which is consistent with the observed incipient but not fully developed Chern insulator gap. For T = 50 K and above, R_{yx} significantly deviates from the quantized value and the crossing branch is completely detached from the bulk valence band at B = 9 T.

These results suggest that below T_N, the FM ordered moments induce a large exchange interaction in a conduction sub-band, which fully crosses the bulk valence band above 7 T, leading to a robust Chern insulator gap. While the long-range ordering of Mn moments disappears at temperatures slightly above T_N, sufficiently large magnetic fields can still align the moments to introduce an incipient Chern insulator state, albeit one much weaker than the state which exists below T_N. Our results highlight that to achieve a comprehensive understanding of the topological physics in this new Chern magnet, it is necessary to combine measurements of local and bulk electronic properties with a careful examination of magnetic states. With a multitude of possible topological phases and magnetic orders in $MnBi_2Te_4$ and related topological magnets,[19−21,26−29] our work paves the way toward a full realization of their potential as a platform to study topological phase transitions and to engineer Chern numbers in Chern insulators via external control knobs.

■ ASSOCIATED CONTENT

Supporting Information

The Supporting Information is available free of charge at https://pubs.acs.org/doi/10.1021/acs.nanolett.0c05117.

Methods, atomic force microscopy measurements, transport and RMCD measurements, evolution of edge states, temperature dependence, and transport measurements for determination of Néel temperature (PDF)

https://dx.doi.org/10.1021/acs.nanolett.0c05117
Nano Lett. 2021, 21, 2544−2550

AUTHOR INFORMATION

Corresponding Authors

Jiaqiang Yan − *Materials Science and Technology Division, Oak Ridge National Laboratory, Oak Ridge, Tennessee 37831, United States; Department of Materials Science and Engineering, University of Tennessee, Knoxville, Tennessee 37996, United States*; Email: yanj@ornl.gov

Cui-Zu Chang − *Department of Physics, The Pennsylvania State University, University Park, Pennsylvania 16802, United States*; orcid.org/0000-0003-3515-2955; Email: cxc955@psu.edu

Yong-Tao Cui − *Department of Physics and Astronomy, University of California, Riverside, California 92521, United States*; orcid.org/0000-0002-8015-1049; Email: yongtao.cui@ucr.edu

Xiaodong Xu − *Department of Physics, University of Washington, Seattle, Washington 98195, United States; Department of Materials Science and Engineering, University of Washington, Seattle, Washington 98195, United States*; orcid.org/0000-0003-0348-2095; Email: xuxd@uw.edu

Authors

Dmitry Ovchinnikov − *Department of Physics, University of Washington, Seattle, Washington 98195, United States*; orcid.org/0000-0002-8971-1639

Xiong Huang − *Department of Physics and Astronomy, University of California, Riverside, California 92521, United States; Department of Materials Science and Engineering, University of California, Riverside, California 92521, United States*; orcid.org/0000-0003-2035-8387

Zhong Lin − *Department of Physics, University of Washington, Seattle, Washington 98195, United States*

Zaiyao Fei − *Department of Physics, University of Washington, Seattle, Washington 98195, United States*; orcid.org/0000-0002-5433-2778

Jiaqi Cai − *Department of Physics, University of Washington, Seattle, Washington 98195, United States*

Tiancheng Song − *Department of Physics, University of Washington, Seattle, Washington 98195, United States*; orcid.org/0000-0002-6845-6624

Minhao He − *Department of Physics, University of Washington, Seattle, Washington 98195, United States*

Qianni Jiang − *Department of Physics, University of Washington, Seattle, Washington 98195, United States*

Chong Wang − *Department of Physics, Carnegie Mellon University, Pittsburgh, Pennsylvania 15213, United States*

Hao Li − *School of Materials Science and Engineering, Tsinghua University, Beijing 100084, People's Republic of China*; orcid.org/0000-0002-9294-9103

Yayu Wang − *Department of Physics, Tsinghua University, Beijing 100084, People's Republic of China*

Yang Wu − *Department of Mechanical Engineering, Tsinghua University, Beijing 100084, People's Republic of China*

Di Xiao − *Department of Physics, Carnegie Mellon University, Pittsburgh, Pennsylvania 15213, United States*

Jiun-Haw Chu − *Department of Physics, University of Washington, Seattle, Washington 98195, United States*

Complete contact information is available at: https://pubs.acs.org/10.1021/acs.nanolett.0c05117

Author Contributions

D.O., X.H., Z.L., and Z.F. contributed equally to the work. X.X., Y.-T.C., C.-Z.C., J.Y., J.-H.C., and D.X. supervised the project. D.O., Z.L., Z.F., and J.C. fabricated devices and performed transport and optical measurements, assisted by T.S., M.H., and Q.J. X.H. performed MIM measurements. C.W. and D.X. provided theoretical support. J.Y. as well as H.L., Y. Wang, and Y. Wu provided and characterized bulk crystals separately. All authors contributed to data analysis. D.O., X.X., Y.-T.C., C.-Z.C., and D.X. wrote the manuscript with inputs from all authors.

Notes

The authors declare no competing financial interest.

The data sets generated and/or analyzed during this study are available from the corresponding author upon reasonable request.

ACKNOWLEDGMENTS

We thank David Cobden and Matthew Yankowitz for helpful discussions, Bevin Huang for initial assistance in RMCD measurements, Jonathan Kephart for advice on fabrication, Anna Isaeva and Zhiqiang Mao who separately provided crystals for testing, and Jordan Fonseca and Eric Anderson for proofreading this manuscript. The work on topological magnetism was solely supported as part of Programmable Quantum Materials, an Energy Frontier Research Center funded by the U.S. Department of Energy (DOE), Office of Science, Basic Energy Sciences (BES), under Award DE-SC0019443. Magneto-optical spectroscopy measurement is partially supported by DOE BES Award DE-SC0018171. Device fabrication and part of the transport measurement are supported by the AFOSR MURI program, Grant No. FA9550-19-1-0390. We also acknowledge the use of the facilities and instrumentation supported by NSF MRSEC Grant No. DMR-1719797. J.Y. acknowledges support from the U.S. Department of Energy, Office of Science, Basic Energy Sciences, Materials Sciences and Engineering Division. C.-Z.C. acknowledges the support from ARO Young Investigator Program Award (W911NF1810198) and the Gordon and Betty Moore Foundation's EPiQS Initiative (Grant No. GBMF9063). X.H. and Y.-T.C. acknowledge support from NSF under Award DMR-2004701, the Hellman Fellowship award, and the seed fund from SHINES, an EFRC funded by DOE BES under Award DE-SC0012670. H.L., Y. Wu, and Y. Wang were supported by NSFC Grant Nos. 21975140 and 51991313. X.X. and J.-H.C. acknowledge the support from the State of Washington funded Clean Energy Institute. Computing time is provided by BRIDGES at the Pittsburgh Supercomputer Center (Grant No. DMR200085) under the Extreme Science and Engineering Discovery Environment (XSEDE) supported by NSF (Grant No. ACI-1548562).

REFERENCES

(1) Haldane, F. D. M. Model for a Quantum Hall-Effect without Landau Levels: Condensed-Matter Realization of the "Parity Anomaly". *Phys. Rev. Lett.* **1988**, *61* (18), 2015−2018.

(2) Weng, H. M.; Yu, R.; Hu, X.; Dai, X.; Fang, Z. Quantum Anomalous Hall Effect and Related Topological Electronic States. *Adv. Phys.* **2015**, *64* (3), 227−282.

(3) Chang, C. Z.; Zhang, J. S.; Feng, X.; Shen, J.; Zhang, Z. C.; Guo, M. H.; Li, K.; Ou, Y. B.; Wei, P.; Wang, L. L.; Ji, Z. Q.; Feng, Y.; Ji, S. H.; Chen, X.; Jia, J. F.; Dai, X.; Fang, Z.; Zhang, S. C.; He, K.; Wang, Y. Y.; Lu, L.; Ma, X. C.; Xue, Q. K. Experimental Observation of the Quantum Anomalous Hall Effect in a Magnetic Topological Insulator. *Science* **2013**, *340* (6129), 167−170.

(4) Chang, C. Z.; Zhao, W. W.; Kim, D. Y.; Zhang, H. J.; Assaf, B. A.; Heiman, D.; Zhang, S. C.; Liu, C. X.; Chan, M. H. W.; Moodera, J.

S. High-Precision Realization of Robust Quantum Anomalous Hall State in a Hard Ferromagnetic Topological Insulator. *Nat. Mater.* **2015**, *14* (5), 473−477.
(5) Checkelsky, J. G.; Yoshimi, R.; Tsukazaki, A.; Takahashi, K. S.; Kozuka, Y.; Falson, J.; Kawasaki, M.; Tokura, Y. Trajectory of the Anomalous Hall Effect towards the Quantized State in a Ferromagnetic Topological Insulator. *Nat. Phys.* **2014**, *10* (10), 731−736.
(6) Kou, X. F.; Guo, S. T.; Fan, Y. B.; Pan, L.; Lang, M. R.; Jiang, Y.; Shao, Q. M.; Nie, T. X.; Murata, K.; Tang, J. S.; Wang, Y.; He, L.; Lee, T. K.; Lee, W. L.; Wang, K. L. Scale-Invariant Quantum Anomalous Hall Effect in Magnetic Topological Insulators beyond the Two-Dimensional Limit. *Phys. Rev. Lett.* **2014**, *113* (13), 137201.
(7) Grauer, S.; Schreyeck, S.; Winnerlein, M.; Brunner, K.; Gould, C.; Molenkamp, L. W. Coincidence of Superparamagnetism and Perfect Quantization in the Quantum Anomalous Hall State. *Phys. Rev. B: Condens. Matter Mater. Phys.* **2015**, *92* (20), 201304.
(8) Mogi, M.; Yoshimi, R.; Tsukazaki, A.; Yasuda, K.; Kozuka, Y.; Takahashi, K. S.; Kawasaki, M.; Tokura, Y. Magnetic Modulation Doping in Topological Insulators toward Higher-Temperature Quantum Anomalous Hall Effect. *Appl. Phys. Lett.* **2015**, *107* (18), 182401.
(9) Zhao, Y.-F.; Zhang, R.; Mei, R.; Zhou, L.-J.; Yi, H.; Zhang, Y.-Q.; Yu, J.; Xiao, R.; Wang, K.; Samarth, N.; Chan, M. H. W.; Liu, C.-X.; Chang, C.-Z. Tuning Chern Number in Quantum Anomalous Hall Insulators. *Nature* **2020**, *588*, 419−423.
(10) Serlin, M.; Tschirhart, C. L.; Polshyn, H.; Zhang, Y.; Zhu, J.; Watanabe, K.; Taniguchi, T.; Balents, L.; Young, A. F. Intrinsic quantized anomalous Hall effect in a moiré heterostructure. *Science* **2020**, *367* (6480), 900−903.
(11) Chen, G. R.; Sharpe, A. L.; Fox, E. J.; Zhang, Y. H.; Wang, S. X.; Jiang, L. L.; Lyu, B. S.; Li, H. Y.; Watanabe, K.; Taniguchi, T.; Shi, Z. W.; Senthil, T.; Goldhaber-Gordon, D.; Zhang, Y. B.; Wang, F. Tunable correlated Chern insulator and ferromagnetism in a moire superlattice. *Nature* **2020**, *579*, 56−61.
(12) Sharpe, A. L.; Fox, E. J.; Barnard, A. W.; Finney, J.; Watanabe, K.; Taniguchi, T.; Kastner, M. A.; Goldhaber-Gordon, D. Emergent Ferromagnetism near Three-Quarters Filling in Twisted Bilayer Graphene. *Science* **2019**, *365*, 605−608.
(13) Otrokov, M. M.; Klimovskikh, I. I.; Bentmann, H.; Estyunin, D.; Zeugner, A.; Aliev, Z. S.; Gass, S.; Wolter, A. U. B.; Koroleva, A. V.; Shikin, A. M.; Blanco-Rey, M.; Hoffmann, M.; Rusinov, I. P.; Vyazovskaya, A. Y.; Eremeev, S. V.; Koroteev, Y. M.; Kuznetsov, V. M.; Freyse, F.; Sanchez-Barriga, J.; Amiraslanov, I. R.; Babanly, M. B.; Mamedov, N. T.; Abdullayev, N. A.; Zverev, V. N.; Alfonsov, A.; Kataev, V.; Buchner, B.; Schwier, E. F.; Kumar, S.; Kimura, A.; Petaccia, L.; Di Santo, G.; Vidal, R. C.; Schatz, S.; Kissner, K.; Unzelmann, M.; Min, C. H.; Moser, S.; Peixoto, T. R. F.; Reinert, F.; Ernst, A.; Echenique, P. M.; Isaeva, A.; Chulkov, E. V. Prediction and observation of an antiferromagnetic topological insulator. *Nature* **2019**, *576* (7787), 416−422.
(14) Gong, Y.; Guo, J.; Li, J.; Zhu, K.; Liao, M.; Liu, X.; Zhang, Q.; Gu, L.; Tang, L.; Feng, X.; Zhang, D.; Li, W.; Song, C.; Wang, L.; Yu, P.; Chen, X.; Wang, Y.; Yao, H.; Duan, W.; Xu, Y.; Zhang, S.-C.; Ma, X.; Xue, Q.-K.; He, K. Experimental Realization of an Intrinsic Magnetic Topological Insulator. *Chin. Phys. Lett.* **2019**, *36*, 076801.
(15) Deng, Y.; Yu, Y.; Shi, M.; Guo, Z.; Xu, Z.; Wang, J.; Chen, X.; Zhang, Y. Quantum anomalous Hall effect in intrinsic magnetic topological insulator. *Science* **2020**, *367*, 895−900.
(16) Liu, C.; Wang, Y. C.; Li, H.; Wu, Y.; Li, Y. X.; Li, J. H.; He, K.; Xu, Y.; Zhang, J. S.; Wang, Y. Y. Robust axion insulator and Chern insulator phases in a two-dimensional antiferromagnetic topological insulator. *Nat. Mater.* **2020**, *19* (5), 522−527.
(17) Ge, J.; Liu, Y.; Li, J.; Li, H.; Luo, T.; Wu, Y.; Xu, Y.; Wang, J. High-Chern-Number and High-Temperature Quantum Hall Effect without Landau Levels. *Natl. Sci. Rev.* **2020**, *7*, 1280−1287.
(18) Liu, C.; Wang, Y.; Yang, M.; Mao, J.; Li, H.; Li, Y.; Li, J.; Zhu, H.; Wang, J.; Li, L.; Wu, Y.; Xu, Y.; Zhang, J.; Wang, Y. Helical Chern insulator phase with broken time-reversal symmetry in $MnBi_2Te_4$. *arXiv (Condensed Matter: Mesoscale and Nanoscale Physics)*, 2020. arXiv:2001.08401. https://arxiv.org/abs/2001.08401 (accessed 2021-03-08).
(19) Otrokov, M. M.; Rusinov, I. P.; Blanco-Rey, M.; Hoffmann, M.; Vyazovskaya, A. Y.; Eremeev, S. V.; Ernst, A.; Echenique, P. M.; Arnau, A.; Chulkov, E. V. Unique Thickness-Dependent Properties of the van der Waals Interlayer Antiferromagnet $MnBi_2Te_4$ Films. *Phys. Rev. Lett.* **2019**, *122* (10), 107202.
(20) Li, J. H.; Li, Y.; Du, S. Q.; Wang, Z.; Gu, B. L.; Zhang, S. C.; He, K.; Duan, W. H.; Xu, Y. Intrinsic Magnetic Topological Insulators in van der Waals Layered $MnBi_2Te_4$-Family Materials. *Sci. Adv.* **2019**, *5* (6), No. eaaw5685.
(21) Zhang, D. Q.; Shi, M. J.; Zhu, T. S.; Xing, D. Y.; Zhang, H. J.; Wang, J. Topological Axion States in the Magnetic Insulator $MnBi_2Te_4$ with the Quantized Magnetoelectric Effect. *Phys. Rev. Lett.* **2019**, *122* (20), 206401.
(22) Yang, S.; Xu, X.; Zhu, Y.; Niu, R.; Xu, C.; Peng, Y.; Cheng, X.; Jia, X.; Xu, X.; Lu, J.; Ye, Y. Odd-even layer-number effect and layer-dependent magnetic phase diagrams in $MnBi_2Te_4$. *arXiv (Condensed Matter: Materials Science)*, 2020. arXiv:2006.07216. https://arxiv.org/abs/2006.07216 (accessed 2021-03-08).
(23) Huang, B.; Clark, G.; Navarro-Moratalla, E.; Klein, D. R.; Cheng, R.; Seyler, K. L.; Zhong, D.; Schmidgall, E.; McGuire, M. A.; Cobden, D. H.; Yao, W.; Xiao, D.; Jarillo-Herrero, P.; Xu, X. D. Layer-Dependent Ferromagnetism in a van der Waals Crystal down to the Monolayer Limit. *Nature* **2017**, *546* (7657), 270−273.
(24) Sass, P. M.; Ge, W. B.; Yan, J. Q.; Obeysekera, D.; Yang, J. J.; Wu, W. D. Magnetic Imaging of Domain Walls in the Antiferromagnetic Topological Insulator $MnBi_2Te_4$. *Nano Lett.* **2020**, *20* (4), 2609−2614.
(25) Cui, Y. T.; Ma, E. Y.; Shen, Z. X. Quartz tuning fork based microwave impedance microscopy. *Rev. Sci. Instrum.* **2016**, *87* (6), 063711.
(26) Hu, C. W.; Gordon, K. N.; Liu, P. F.; Liu, J. Y.; Zhou, X. Q.; Hao, P. P.; Narayan, D.; Emmanouilidou, E.; Sun, H. Y.; Liu, Y. T.; Brawer, H.; Ramirez, A. P.; Ding, L.; Cao, H. B.; Liu, Q. H.; Dessau, D.; Ni, N. A van der Waals antiferromagnetic topological insulator with weak interlayer magnetic coupling. *Nat. Commun.* **2020**, *11* (1), 97.
(27) Wu, J. Z.; Liu, F. C.; Sasase, M.; Ienaga, K.; Obata, Y.; Yukawa, R.; Horiba, K.; Kumigashira, H.; Okuma, S.; Inoshita, T.; Hosono, H. Natural van der Waals heterostructural single crystals with both magnetic and topological properties. *Sci. Adv.* **2019**, *5* (11), No. eaax9989.
(28) Yan, J. Q.; Okamoto, S.; McGuire, M. A.; May, A. F.; McQueeney, R. J.; Sales, B. C. Evolution of structural, magnetic, and transport properties in $MnBi_{2-x}Sb_xTe_4$. *Phys. Rev. B: Condens. Matter Mater. Phys.* **2019**, *100* (10), 104409.
(29) Yan, J. Q.; Liu, Y. H.; Parker, D.; Wu, Y.; Aczel, A. A.; Matsuda, M.; McGuire, M. A.; Sales, B. C. A-type antiferromagnetic order in $MnBi_4Te_7$ and $MnBi_6Te_{10}$ single crystals. *Phys. Rev. Mater.* **2020**, *4* (5), 054202.

https://dx.doi.org/10.1021/acs.nanolett.0c05117
Nano Lett. 2021, 21, 2544−2550